AIP | Review of Scientific Instruments

# Optical design of the short pulse x-ray imaging and microscopy time-angle correlated diffraction beamline at the Advanced Photon Source

R. Reininger, E. M. Dufresne, M. Borland, M. A. Beno, L. Young et al.

Citation: Rev. Sci. Instrum. **84**, 053103 (2013); doi: 10.1063/1.4804197
View online: http://dx.doi.org/10.1063/1.4804197
View Table of Contents: http://rsi.aip.org/resource/1/RSINAK/v84/i5
Published by the American Institute of Physics.

# Optical design of the short pulse x-ray imaging and microscopy time-angle correlated diffraction beamline at the Advanced Photon Source

R. Reininger,[1] E. M. Dufresne,[1] M. Borland,[1] M. A. Beno,[1] L. Young,[1] K.-J. Kim,[1] and P. G. Evans[2]
[1]*Advanced Photon Source, Argonne National Laboratory, Argonne, Illinois 60439, USA*
[2]*Department of Materials Science and Engineering, University of Wisconsin, Madison, Wisconsin 53706, USA*

(Received 17 January 2013; accepted 22 April 2013; published online 10 May 2013)

The short pulse x-ray imaging and microscopy beamline is one of the two x-ray beamlines that will take full advantage of the short pulse x-ray source in the Advanced Photon Source (APS) upgrade. A horizontally diffracting double crystal monochromator which includes a sagittally focusing second crystal will collect most of the photons generated when the chirped electron beam traverses the undulator. A Kirkpatrick-Baez mirror system after the monochromator will deliver to the sample a beam which has an approximately linear correlation between time and vertical beam angle. The correlation at the sample position has a slope of 0.052 ps/$\mu$rad extending over an angular range of 800 $\mu$rad for a cavity deflection voltage of 2 MV. The expected time resolution of the whole system is 2.6 ps. The total flux expected at the sample position at 10 keV with a 0.9 eV energy resolution is $5.7 \times 10^{12}$ photons/s at a spot having horizontal and vertical full width at half maximum of 33 $\mu$m horizontal by 14 $\mu$m vertical. This new beamline will enable novel time-dispersed diffraction experiments on small samples using the full repetition rate of the APS. © *2013 AIP Publishing LLC*. [http://dx.doi.org/10.1063/1.4804197]

## I. INTRODUCTION

A significant upgrade of the Advanced Photon Source (APS) at Argonne National Laboratory is planned to occur during 2013–2020. Part of this upgrade includes the short pulse x-ray (SPX) source; the implementation of the deflecting-cavity scheme proposed by Zholents *et al.*[1] for the production of intense, tunable, few-picosecond x-ray pulses with high repetition rates. The experimental facilities associated with the SPX source will combine picosecond temporal resolution with atomic-scale structural precision, elemental and chemical specificity, and nanoscale spatial resolution to enable an understanding of the relationship between structure and function in complex systems. Dynamical processes are typically initiated with optical laser pulses, which can be used to generate radiation from the terahertz through the extreme ultraviolet for excitation of electronic states and lattice degrees of freedom. Such excitations can drive systems through phase transitions (e.g., melting, ferroic, and superconducting transitions) and can create metastable states not present in thermal equilibrium. The excitation can also take the form of pulsed electric fields applied to devices or of optically induced mechanical transients.

The SPX Facility is designed to take advantage of the unique features of the SPX source, the most important of which is the production of short-duration x-ray pulses at the full 6.5 MHz repetition rate of the APS. The high average x-ray flux is conveniently parceled in bunches of $10^4$–$10^6$ x-rays photons in each ps-duration pulse. Instruments using the SPX source offer the opportunity to probe dynamics on an atomic length-scale via diffraction, with minimal x-ray induced perturbation of the system. The photon energy and x-ray spot size can be readily and independently chosen for specific experiments at the beamlines within the SPX Facility. The advantageous timing structure of the APS storage ring makes it straightforward to select a variable experimental repetition rate as required for different systems. For example, the combination of the short pulse duration of the SPX source combined with the high repetition rate of the APS will be particularly valuable for the study of high-frequency nanoscale devices operating at frequencies approaching 1 THz.

The SPX Facility consists of three independent beamlines: SPXSS (Short Pulse X-ray Scattering and Spectroscopy); SPXIM (Short Pulse X-ray Imaging and Microscopy); and the SPSXS (Short Pulse X-ray Soft X-ray Spectroscopy). These three beamlines are located between the two rf deflection cavities[1,2] that provide chirped electron pulses. The propagation of the APS storage ring's electron beam through the cavities imposes a correlation between the longitudinal position of an electron in the bunch and its vertical momentum. The x-ray radiation emitted during the electron propagation through an undulator or bending magnet preserves the correlation and a short pulse can be selected out simply with a pair of slits. The SPXIM beamline described in this paper is unique in that it will also allow the capture and refocusing of the entire vertical fan of radiation to provide time-dispersed capabilities with few-picosecond resolution.

The principal goal of the short pulse x-ray imaging and microscopy beamline is to provide picosecond-duration, high-repetition-rate pulses of tunable, polarized x-ray radiation for imaging and microscopy experiments in condensed matter physics and materials science. The picosecond time scale has unique importance because it is an excellent match for structural dynamics in nanoscale systems. These areas are of technological relevance as well as of fundamental interest. The facilities described here will enable ground-breaking experiments in a range of scientific problems. Scattering, imaging,

 

and spectroscopy probes will be particularly valuable in five areas:

1. Dynamics in ferroic materials. In nanomagnetic, ferroelectric, and multiferroic systems the competition of multiple long-range order parameters leads to new opportunities to manipulate remnant electrical polarization and magnetic order, and to drive materials into structural states far from equilibrium.[3–5]
2. High-frequency materials and devices. Structural phenomena have a large impact on optical and mechanical properties in the 10 GHz–1 THz range, but the detailed origins of these phenomena are only beginning to be understood and exploited.[6–8]
3. Thermal and atomic transport at interfaces. Many critical processes in the transport of heat across interfaces and the motion of solid-liquid interfaces occur at timescales that have previously been inaccessible to precise structural probes based on x-ray diffraction and scattering.[9–11]
4. Dynamics of fundamental excitations. The structural features associated with the fundamental excitations of solids and the cascade of energy between these excitations are presently difficult to probe because appropriate time-resolved structural techniques do not exist.[12,13]
5. Picosecond imaging. The SPX facilities provide the capability to form picosecond duration images of ultrafast processes and, via the divergence of the SPX source, single-shot images of long-length-scale 1D phenomena including the dynamics of fluid jets and fluid-interface interactions.[14,15]

The SPXIM beamline uses x-ray radiation produced by a hard x-ray insertion device (ID) and consists of two end stations; one that uses the full vertical fan to enable novel time-dispersed diffraction capabilities and to record a time history of 70 ps with few-ps resolution; and a second one that houses a zone-plate-based microscope capable of focusing the monochromatic radiation to approximately 100 nm. The SPX Facility will be equipped with high-power and high-repetition rate femtosecond lasers, similar to those already existing at the Advanced Photon Source[16] that will deliver beams to the SPXIM and SPXSS beamlines. This paper describes the source, x-ray optics, and expected performance of the SPXIM beamline relevant to the time-dispersed diffraction experiments.

## II. SOURCE

The SPXIM beamline will be located on the 6-ID port at the APS. Its main operation range will be between 7 and 14 keV, but the beamline is designed to cover the energy range between 4.6 and 24.9 keV. To optimize the flux in the full energy range, a 2.1-m-long revolver undulator with 27 mm and 30 mm periods was selected. As shown in Fig. 1, the 27 mm period device gives continuous tuning over the entire energy range in the first harmonic, and the 30 mm period provides enhanced flux below 7 keV in the first harmonic and above 13 keV in the third harmonic.

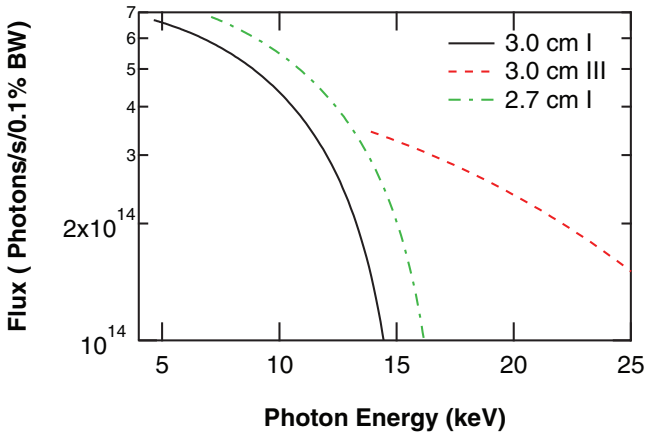


FIG. 1. Total flux emitted in the central cone by the 2.1 m long revolver undulator in the first (solid line) and third harmonic (dashed line) when using the 3 cm period device and emitted in the first harmonic (dotted-dashed line) by the 2.7 cm device. The current in the storage ring is 150 mA.

The simulations described below consider the propagation of the radiation emitted by a chirped electron pulse passing through the 2.7 cm period undulator. The calculations assume that the gap of the undulator is tuned to emit 10 keV on axis. The undulator is located 1.2 m downstream of the center of the 6 ID straight section. The statistical representation of the radiation was obtained in four steps. In the first step, the accelerator simulation code ELEGANT[17] is used to determine the equilibrium properties of $10^6$ electrons at the center of the undulator, sampling the horizontal and vertical phase space as well as time (position along the electron bunch). The electron energy spread (<0.1%) is not included in the simulations since its contribution to the spectra-angular distribution is much smaller than the contribution due to the number of periods in the undulator. In the second step, the angular distribution of the undulator radiation from a single electron was obtained using the SPECTRA code[18] over a wide angular range that includes the first harmonic radiation, which is emitted in the forward direction ("central cone"), as well as the radiation emitted (also at 10 keV) in a concentric ring centered around the central cone.[19] Since the SPECTRA code does not generate the size of the photon beam due to a single electron, the third step involves a statistical sampling of the size of the central cone and that of the second harmonic (SH) ring at the center of the insertion device. For the central cone we assumed a Gaussian distribution for the size with a RMS value[20] of $\sigma = \sqrt{2\lambda L}/2\pi = 3.6\ \mu$m, where $\lambda$ is the wavelength and $L$ is the undulator length. Based on the derivation in the Appendix, we used for the size distribution of the second harmonic radiation a Gaussian with a RMS value of $\sigma/(2\sqrt{N}) = 0.2\ \mu$m, where $N$ is the number of undulator periods. In the fourth step, the electron distribution is convoluted with the statistical sampling of the undulator radiation calculated in steps two and three. Twenty-four-bunch mode with a 41 ps RMS electron bunch length was assumed in the ELEGANT calculation.

Figure 2 shows the correlation between time and the vertical angle of the radiation emitted at 10 keV over the full horizontal fan of almost 200 $\mu$rad. We have chosen a

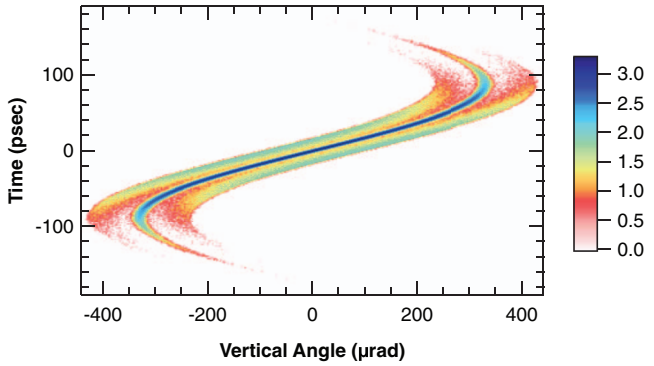


FIG. 2. Log (base 10) of the number of rays as a function of time and vertical angle when accepting the full horizontal fan (see text).

logarithm representation of the $10^6$ rays in the figure to illustrate the correlation and show the significant variation in the number of rays displayed. Figure 3 shows the same correlation when the horizontal acceptance is limited to 50 $\mu$rad, which contains 25% less rays than Fig. 2. As seen in Fig. 3 and less clearly in Fig. 2, there are three bands. The central one corresponds to the radiation emitted by the undulator in the first harmonic, whereas the other two bands correspond to the off-axis radiation due to the second harmonic, nominally at 20 keV, which is red shifted in energy to 10 keV at an angle equal to $\pm\gamma^{-1}\sqrt{1+k^2/2} = \pm 96$ $\mu$rad.[19] Evidently, the rays not accepted by the horizontal aperture are mostly those in the second harmonic ring. The fraction of lost rays is in agreement with the ratio between the integrated intensity of the SH and the integrated intensity of the central cone obtained using the angular distribution of the single electron emission given by SPECTRA.

Figure 3 demonstrates that the correlation between time ($t$) and vertical angle is almost linear for the first and second harmonic radiation over approximately $\pm 200$ $\mu$rad and $|t|$ <40 ps with a slope of 0.18 ps/$\mu$rad. The time resolution in the limit of zero divergence for the radiation emitted in the central cone is determined by the properties of the electron beam and the divergence of the photon beam. Its value, 2.6 ps full width at half maximum (FWHM), is obtained from a narrow angular range around zero $\mu$rad in the trace representing the central cone radiation in Fig. 3. However, it should be pointed out that the presence of the SH means a time resolution degradation since these photons arrive at $\pm 96$ $\mu$rad $\times$ 0.18 ps/$\mu$rad= $\pm 17$ ps for the same vertical angle. Another factor deteriorating the time resolution is the fraction of rays with $|t| > 40$ ps in the $\pm 200$ $\mu$rad vertical angle range, due to the electrons in the "back-chirped" pulse. Their effect is relatively small since their flux is less than 0.1% of the flux in the $\pm 200$ $\mu$rad and $|t| < 40$ ps window.

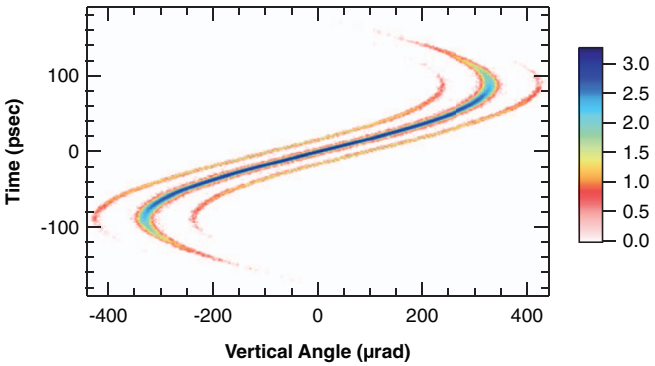


FIG. 3. Log (base 10) of number of rays as a function of time and vertical angle when accepting 50 $\mu$rad horizontally.

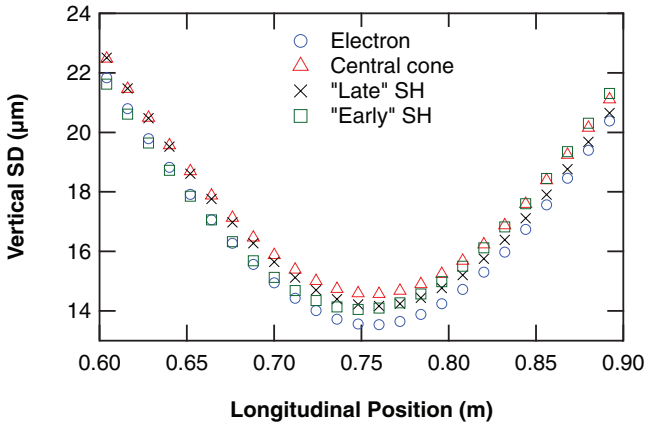


FIG. 4. SD of the vertical size of the electron distribution (○) and its convolution with the photon beam (△: central cone; ×: SH late pulse; □: SH early pulse) as a function of the longitudinal distance. Zero meter corresponds to the center of the undulator.

The linear dependence between time and vertical angle was used to separate the rays of the first and second harmonic radiation over the $\pm 200$ $\mu$rad vertical angle range. The rays belonging to each band were then propagated (using basic ray-tracing) as a function of the longitudinal position relative to the center of the insertion device. Figure 4 shows the standard deviation (SD) of the vertical size of the electron beam and that of the three bands of the photon beam as a function of the longitudinal position. Each one of the traces in the figure was fitted with $\sqrt{((x-x_0)\sigma')^2+\sigma_0^2}$, where $x$ is the longitudinal position, $\sigma'$ is the divergence, $\sigma_0$ and $x_0$ are the waist and its position. The fits yield 13.5 $\mu$m, 14.4 $\mu$m, and 14.1 $\mu$m for the waist of the electron beam, the central cone, and the two bands due to the second harmonic radiation, respectively. The waist position of the central cone and the electron coincide at 0.76 m, whereas the waist position of the early SH radiation is a few mm upstream and that of the late SH radiation is a few mm downstream. We note that the waist of the central cone is also at 14.1 $\mu$m when the convolution is done assuming no size for the central cone. The calculation of the horizontal SD yields 272 $\mu$m, which is equal to the horizontal SD of the electron beam located at the center of the 6 ID straight section.

In general, it should be pointed out that the source position and size of the central cone of the undulator radiation depend on the position of the electron beam waist. Furthermore, the source position could vary as a function of the photon energy when the waists of the single electron emission and the waist of the electron beam do not coincide and are comparable in size.[21]

Figure 5 shows the number of rays as a function of time and vertical coordinate at the position of the photon beam

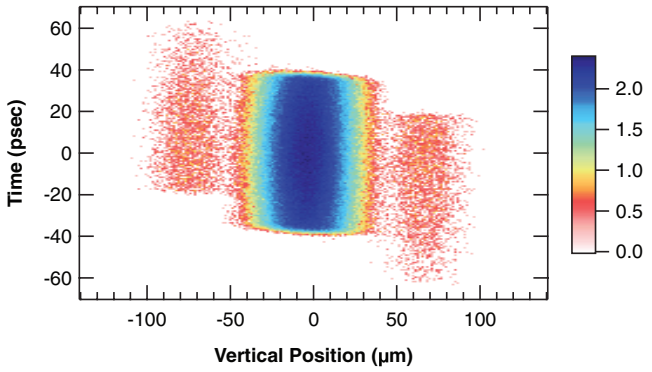


FIG. 5. Log (base 10) of the number of rays as a function of time and vertical position at 0.76 m downstream from the center of the undulator; i.e., where the radiation has its vertical waist.

vertical waist, i.e., at 0.76 m downstream from the center of the undulator. As in Figs. 2 and 3, we have chosen a logarithmic representation for the number of rays to show the three bands and the significant difference in the number of rays in the first and second harmonic. Figure 5 demonstrates that the centers of the second harmonic contributions are separated vertically from the center of the first harmonic radiation by $\pm 96\ \mu\text{rad} \times 0.76\ \text{m} = \pm 73\ \mu\text{m}$ with very little overlap. This important result means that a slit located at an image plane of the vertical waist will significantly reduce the radiation of the second harmonic which arrives at $\pm 17$ ps for the same vertical angle.

## III. OPTICAL LAYOUT

Figure 6 shows the x-ray optical layout of the SPXIM beamline. Table I summarizes the position of the optical elements relative to the center of the straight section. A set of white beam slits specially designed to accept the full vertical beam ($\approx -0.8$ mrad) will be placed at 32 m from the center of the straight section.

A double-crystal monochromator (DCM) with cryogenically cooled Si⟨111⟩ and Si⟨220⟩ crystals will be located downstream of the white beam slits. A similar monochromator is currently in use at beamline 12-ID at the APS. The diffraction plane is horizontal and the monochromator will have a 0.86 m horizontal offset. It will provide monochromatic x-rays with an energy resolution $\Delta E/E$ of $\approx 1 \times 10^{-4}$ with Si⟨220⟩. The design of the similar monochromator at station 12-ID allows it to cover the photon energy range from 7.2 to 14 keV with Si⟨220⟩ crystals. The design of the monochromator takes into consideration the energy range required for experiments and the details of the mechanical bender. The second crystal of the SPXIM monochromator will have a sagittal bender that enables vertical focusing of the full SPX vertical fan with approximately a 2:1 demagnification. Two different crystal orientations will be outfitted to extend the range of photon energies. Energies below 7 keV will be reached using Si⟨111⟩ crystals and energies up to 24.9 keV will use Si⟨333⟩ reflections. The lower energy range will be useful in accessing a wide range of elemental edges for resonant scattering, e.g., the Fe K-edge relevant to some multiferroic materials. Higher energies achieved with Si⟨333⟩ allow higher wavevector coverage and shorter x-ray pulses.[2] Two Si flats crystals ⟨111⟩ and ⟨220⟩ will also be included to bypass the bender for imaging experiments that require preservation of the original time-angle correlation.[14]

TABLE I. Position of the optical elements relative to the straight section center.

| Element | Position (mm) | Note |
|---|---|---|
| Undulator center | 1200 | |
| White beam slits | 32 000 | Up to 25 mm (V) × 3 mm (H) |
| Double crystal | 35 000 | Horizontally diffracting |
| Monochromator | | Second crystal sagittally focusing |
| Timing slits | 54 000 | |
| Elliptical cylinder | 57 000 | Horizontal focusing |
| Elliptical cylinder | 57 700 | Vertical focusing |
| Sample | 60 000 | At 6-circle diffractometer |

The timing slit is located at the vertical focus generated by the sagittally bent monochromator second crystal. As shown in the ray tracings results presented in Sec. IV, a 25 $\mu$m

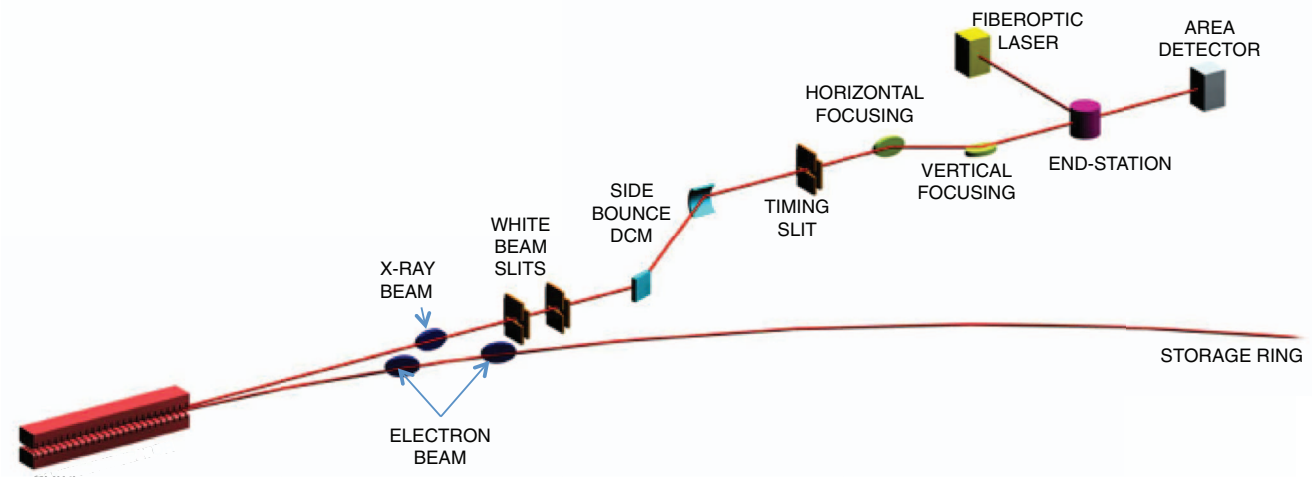


FIG. 6. Optical layout of the SPXIM beamline.

slit allows to filter out the second harmonic photons which have a shifted time-vertical divergence correlation relative to the first harmonic (see Fig. 3).

The first element of the Kirkpatrick-Baez (KB) pair[22] is the horizontally focusing elliptical cylinder that demagnifies the beam along the horizontal direction by a factor of 19. The second mirror of the pair is also an elliptical cylinder imaging the (vertical) slit at the sample position with a demagnification of 1.6. Both mirrors are 0.5-m-long Si substrates dynamically bent and able to operate at angles of incidence optimized for higher order suppression. The KB system will accept most of the horizontal and vertical fans when operating at a grazing angle of 6 mrad. The geometrical acceptance of the KB system will decrease to 33% when operated at the smallest angle of grazing incidence required at 25 keV, ≈3 mrad with a Pt coating.

## IV. RAY TRACINGS

The ray tracings described below were performed with the SHADOW code.[23,24] The source used in the ray tracings consisted of the $10^6$ rays mentioned in Sec. II having a continuous distribution of photon energies between 9.995 and 10.005 keV. An aperture 32 m downstream of the source was set to accept 50 $\mu$rad × 400 $\mu$rad (horizontal × vertical).

The first optical element is a horizontally diffracting Si⟨220⟩ crystal tuned to 10 keV. The second crystal in the double crystal monochromator is also a Si⟨220⟩ crystal. This crystal is sagittally bent (to a radius of 7.6 m) to focus the 10 keV beam along the vertical direction at the slit. The slit is positioned at a distance of 54 m from the center of the straight section. The vertical demagnification is approximately 2:1; not the conventional 3:1 used when a sagittal crystal is used to focus a beam with a larger divergence.[25] The left axis in Fig. 7 shows the intensity as function of the incident energy obtained using SHADOW for two cases: (i) after a flat crystal followed by the sagittally bent crystal and (ii) after the flat crystal followed by a second flat crystal instead of the sagittally bent one. As seen in the figure, the results for the two cases are practically identical; i.e., neither the energy resolution nor the total intensity is affected by the use of the sagittal cylinder. Figure 7 also compares the resolution obtained using SHADOW with the absolute reflectivity (right axis) after two Si⟨220⟩ p reflections of a collimated beam. The FWHM with collimated light is 0.49 eV, half the value obtained from the SHADOW results since the latter includes the broadening of the energy resolution due to horizontal divergence.

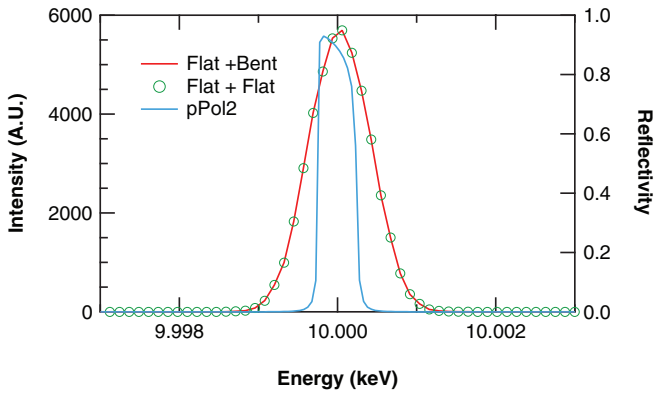


FIG. 7. Energy resolution of a flat Si⟨220⟩ crystal followed by the sagittally bent crystal (red line); two flats (green circles). Right axis: (for trace labeled pPol2) p reflectivity of two flat ⟨220⟩ Si with collimated light.

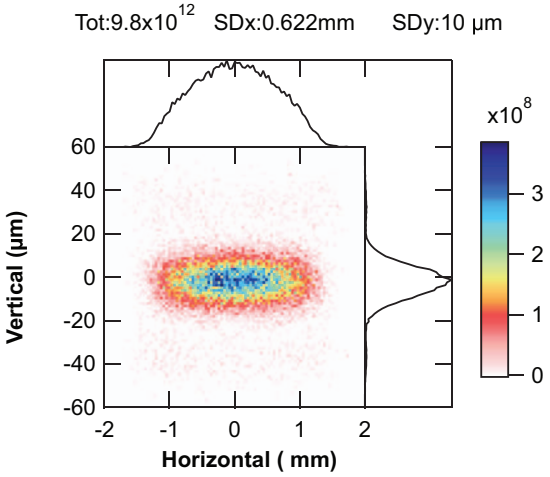


FIG. 8. Flux density (scale in units of photons/s/$\mu$m$^2$) at the slit plane when using the Si⟨220⟩ crystals. The caption above the figure gives the total flux (in units of photons/s) as well as the standard deviations of the beam size along the horizontal and vertical directions.

The photon flux density at the slit plane is presented in Fig. 8. The flux density was obtained from the ray tracings taking into account the flux emitted by the undulator at 10 keV and the transmission of the DCM when using the Si⟨220⟩ crystals. The peak flux density is 3.8 × $10^8$ photons/s/$\mu$m$^2$ at a spot with horizontal and vertical SD values of 0.622 mm and 10 $\mu$m, respectively. The total flux is almost $10^{13}$ photons/s. The histograms in the figure show the intensity distribution along the horizontal and vertical directions. The flux density due to the second harmonic is not clearly seen in the figure but its contribution, which totals less than 4% of the total flux, is visible beyond ≈±25 $\mu$m in the vertical histogram.

The correlation between time and vertical divergence at the sample position with a fully open slit showing the second

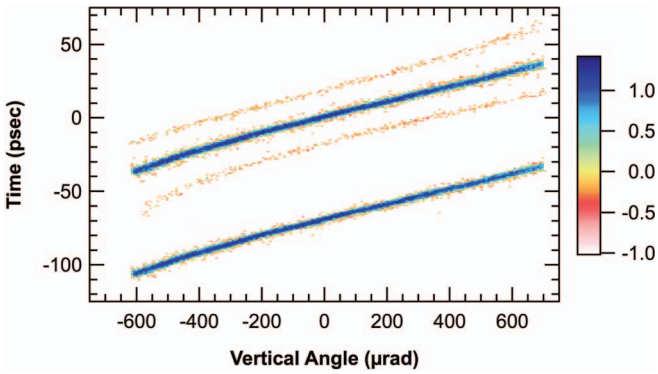


FIG. 9. Log (base 10) of the intensity at the sample position as a function of time and vertical angle. Upper trace (centered around 0 ps): With fully opened vertical slit; lower trace (shifted by −70 ps to make it visible in the figure) after a 25 $\mu$m slit.

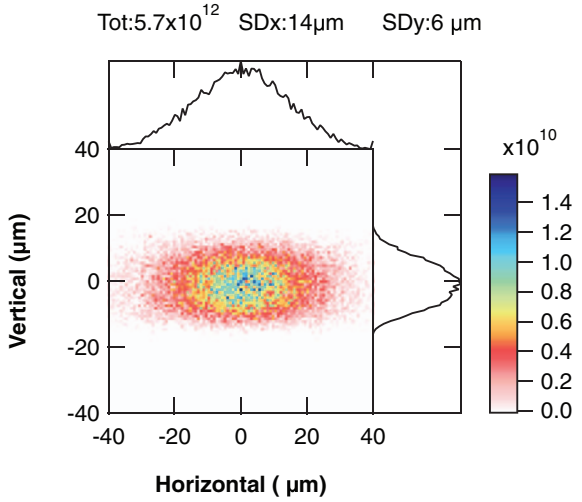


FIG. 10. Flux density (scale in units of photons/s/$\mu$m$^2$) at the sample position at the energy resolution of the Si⟨220⟩ DCM. The caption above the figure as in Fig. 8.

harmonic contributions at earlier and later times is seen in the trace centered at 0 ps in Fig. 9. The lower trace (shifted by −70 ps) demonstrates that a 25 $\mu$m slit completely removes the contribution due to the second harmonic. Not visible in the traces is the contribution due to the back chirped pulse accepted by the beamline since its total contribution at the sample position is less than 0.1%. Figure 9 also shows that the expected total vertical divergence at the sample position is slightly asymmetrical and 1.3 mrad wide. In addition, the figure demonstrates that the time vertical divergence correlation at the sample is almost linear between −200 and 600 $\mu$rad with a slope equal to 0.052 ps/$\mu$rad. From a linear region in the time vertical divergence correlation, one obtains that the time resolution at the sample position in a limit of zero divergence has a FWHM of 2.6 ps, equal to the value obtained in Sec. II. The time resolution due to the pixel size assuming a gated intensified charge-coupled device (ICCD) imaging fluorescence from a single crystal phosphor with a 13 $\mu$m square pixels located at 2 m from the sample is 0.052 ps/$\mu$rad × 13 $\mu$m/2 m = 0.34 ps/pixel. Adding this in quadrature with the time resolution in the limit of zero divergence yields an overall time resolution per pixel of 2.6 ps.

The photon flux density at the sample position including the geometrical and reflectivity losses of the KB mirrors at an angle of 6 mrad and RMS slope errors of 1 $\mu$rad is shown in Fig. 10. The total flux expected at the sample is 5.7 × $10^{12}$ photons/s at a spot having horizontal and vertical SD of 14 $\mu$m and 6 $\mu$m, respectively. RMS slope errors of 0.5 $\mu$rad will lower these values to 13 $\mu$m and 4.5 $\mu$m (horizontal × vertical). The FWHM of the horizontal divergence at the sample is ≈0.5 mrad.

## V. CONCLUSION

The APS upgrade which includes machine improvements, the SPX Source and Facility, several new beamlines, and beamline upgrades has been reviewed and expects approval from the Department of Energy of Critical Decision-2 (CD-2). The SPXIM beamline is designed based on existing technologies and should provide high flux (≈6 × $10^{12}$ photons/s) and a small spot size at the sample over the energy range 5–14 keV. Its uniqueness will be the delivery to the sample of high-repetition-rate pulses of tunable, polarized x-ray radiation with a linear correlation between time and vertical divergence with a 2.6 ps time resolution.

## ACKNOWLEDGMENTS

The Advanced Photon Source, an Office of Science User Facility operated for the U.S. Department of Energy (DOE) Office of Science by Argonne National Laboratory, was supported by the U.S. DOE under Contract No. DE-AC02-06CH11357. We thank Mark Erdmann and Joshua Downey for their contribution to the beamline layout, and Louis Emery and Sarvjit Shastri for helpful discussions. P.E. acknowledges support from the DOE Office of Basic Energy Sciences, Division of Materials Sciences and Engineering under award DE-FG02-10ER46147.

## APPENDIX: BEAM SIZES

In addition to the emission of the fundamental wavelength, $\lambda$, in the forward direction, an undulator also emits the same wavelength in concentric rings at a half angle $\theta_l$, where

$$\theta_l = \frac{1}{\gamma}\sqrt{l\left(1+\frac{K^2}{2}\right)}. \tag{A1}$$

Equation (A1) corresponds to the red-shifted $(l+1)$th harmonic radiation, where $\gamma$ is the electron energy in units of its rest mass energy and $K$ is the undulator parameter. For $l=1$, $\theta_l$ is roughly $2\sqrt{N}$ times larger than the RMS angle of the fundamental emission in the forward direction, $\sigma'$, where $N$ is the number of undulator periods.[19] The width of the ring, $\Delta\theta_l$, is smaller than $\sigma'$ by approximately the same factor.[19] Thus,

$$\theta_l \approx 4N\ \Delta\theta_l \gg \Delta\theta_l. \tag{A2}$$

The source spatial distribution can be determined by Fourier transformation if the electric field $\widetilde{E}$ is known in angular representation. In a simplified model, one can assume that the angular distribution of the electric field is given by

$$\widetilde{E}(\vec{\phi}\,) \propto \exp\left[-\frac{(|\vec{\phi}|-\theta_l)^2}{{\Delta\theta_l}^2}\right], \tag{A3}$$

where $\vec{\phi}$ is a two dimensional angle vector. In spatial coordinates, the electric field is given by

$$E(\vec{x}) \propto \int \widetilde{E}(\vec{\phi}\,)\exp[ik\vec{\phi}\cdot\vec{x}]\,d^2\vec{\phi}. \tag{A4}$$

Using the polar coordinates of the angular variables, one obtains

$$E(\vec{x}) \propto \int_{-\pi}^{\pi}\int_{0}^{\infty} \widetilde{E}(\vec{\phi}\,)\exp[ik\vec{\phi}\cdot\vec{x}]\,|\vec{\phi}|\,d|\vec{\phi}|\,d\chi. \tag{A5}$$

Changing the coordinate $|\vec{\phi}| = \nu + \theta_l$ yields

$$E(\vec{x}) \propto \int_{-\pi}^{\pi} \int_{-\theta_l}^{\infty} \exp\left[-\frac{\nu^2}{\Delta{\theta_l}^2}\right] \exp[ik(\nu+\theta_l)\, r\cos\chi] \times(\nu+\theta_l) d\nu d\chi. \quad \text{(A6)}$$

From Eq. (A2) one can replace the lower limit of the $\nu$ integral to $-\infty$. Considering that the $\nu$ integral comes from a region much smaller than $\theta_l$, the integral over $\nu$ can be performed assuming that the first term is a Dirac delta function with the simple result

$$E(\vec{x}) \propto \approx \int_{-\pi}^{\pi} \exp[ik\theta_l\, r\cos\chi]\, d\chi \propto J_0(kr\theta_l), \quad \text{(A7)}$$

where $J_0$ is a Bessel function of the first kind.

The RMS value, $\Sigma$, of the central peak in the spatial distribution of $|E(\vec{x})|^2$ is

$$\Sigma \approx \frac{1}{k\theta_l} = \frac{\lambda}{2\pi\theta_l} \approx \frac{\lambda}{4\pi\sqrt{N}\sigma'} \approx \frac{\sigma}{2\sqrt{N}}, \quad \text{(A8)}$$

where $\sigma$ is the RMS size of the forward radiation, and we have assumed $\sigma \times \sigma' \approx \lambda/2\pi$.[20]


[1] A. Zholents, P. Heimann, M. Zolotorev, and J. Byrd, Nucl. Instrum. Methods Phys. Res. A **425**, 385 (1999).
[2] M. Borland, Phys. Rev. ST Accel. Beams **8**, 074001 (2005).
[3] D. Daranciang, M. Highland, H. Wen, S. Young, N. Brandt, H. Hwang, M. Vattilana, M. Nicoul, F. Quirin, J. Goodfellow *et al.*, Phys. Rev. Lett. **108**, 087601 (2012).
[4] J. Y. Jo, P. Chen, R. J. Sichel, S. J. Callori, J. Sinsheimer, E. M. Dufresne, M. Dawber, and P. G. Evans, Phys. Rev. Lett. **107**, 055501 (2011).
[5] P. Chen, J. Y. Jo, H. N. Lee, E. M. Dufresne, S. M. Nakhmanson, and P. G. Evans, New J. Phys. **14**, 013034 (2012).
[6] M. Tomes and T. Carmon, Phys. Rev. Lett. **102**, 113601 (2009).
[7] X. Sun, J. Zheng, M. Poot, C. W. Wong, and H. X. Tang, Nano Lett. **12**, 2299 (2012).
[8] B. Ferguson and X. C. Zhang, Nature Mater. **1**, 26 (2002).
[9] M. A. Scarpulla, O. D. Dubon, K. M. Yu, O. Monteiro, M. R. Pillai, M. J. Aziz, and M. C. Ridgway, Appl. Phys. Lett. **82**, 1251 (2003).
[10] Y. Wu and P. Yang, Adv. Mater. **13**, 520 (2001).
[11] M. Hu, D. Poulikakos, C. P. Grigoropoulos, and H. Pan, J. Chem. Phys. **132**, 164504 (2010).
[12] M. Trigo, J. Chen, M. P. Jiang, W. L. Mao, S. C. Riggs, M. C. Shapiro, I. R. Fisher, and D. A. Reis, Phys. Rev. B **85**, 081102 (2012).
[13] H. Marciniak, M. Fiebig, M. Huth, S. Schiefer, B. Nickel, F. Selmaier, and S. Lochbrunner, Phys. Rev. Lett. **99**, 176402 (2007).
[14] A. G. MacPhee, M. W. Tate, C. F. Powell, Y. Yue, M. J. Renzi, A. Ercan, S. Narayanan, E. Fontes, J. Walther, J. Schaller *et al.*, Science **295**, 1261 (2002).
[15] M. Reyssat, J. M. Yeomans, and D. Quéré, Europhys. Lett. **81**, 26006 (2008).
[16] A. M. March, A. Stickrath, G. Doumy, E. P. Kanter, B. Krässig, S. H. Southworth, K. Attenkofer, C. A. Kurtz, L. X. Chen, and L. Young, Rev. Sci. Instrum. **82**, 073110 (2011).
[17] M. Borland, "elegant: A Flexible SDDS-Compliant Code for Accelerator Simulation," Advanced Photon Source LS-287, September 2000.
[18] T. Tanaka and H. Kitamura, J. Synchrotron Radiat. **8**, 1221 (2001).
[19] K. J. Kim, AIP Conf. Proc. **184**, 565 (1989).
[20] P. Elleaume, in *Undulators, Wigglers and their Applications*, edited by H. Onuki, and P. Elleaume (Taylor and Francis, London, 2003).
[21] R. Reininger, Nucl. Instrum. Methods Phys. Res. A **649**, 139 (2011).
[22] P. Kirkpatrick and A. V. Baez, J. Opt. Soc. Am. **38**, 766 (1948).
[23] C. Welnak, G. J. Chen, and F. Cerrina, Nucl. Instrum. Methods Phys. Res. A **347**, 344 (1994).
[24] M. Sanchez del Rio, N. Canestrari, F. Jiang, and F. Cerrina, J. Synchrotron Radiat. **18**, 708 (2011).
[25] C. J. Sparks, Jr., B. S. Borie, and J. B. Hastings, Nucl. Instrum. Methods Phys. Res. **172**, 237 (1980).